Journal of Comparative Neurology

WILEY

JCN RESEARCH IN SYSTEMS NEUROSCIENCE THE JOURNAL OF COMPARATIVE NEUROLOGY

RESEARCH ARTICLE OPEN ACCESS

Cellular Organization and Migration Pathways of the Ventricular–Subventricular Zone in the Juvenile Swine Brain (*Sus scrofa domesticus*)

Lucía Inés Torrijos-Saiz[1] | Júlia Freixes[2] | Ester Desfilis[2] | Loreta Medina[2] | Kazunobu Sawamoto[3,4] | José Manuel García-Verdugo[1] | Vicente Herranz-Pérez[5]

[1]Laboratory of Comparative Neurobiology, Cavanilles Institute of Biodiversity and Evolutionary Biology, University of Valencia – CIBERNED-ISCIII, Paterna, Spain | [2]Laboratory of Evolutionary and Developmental Neurobiology, University of Lleida and Lleida's Institute for Biomedical Research – Dr. Pifarré Foundation (IRBLleida), Lleida, Spain | [3]Department of Developmental and Regenerative Neurobiology, Institute of Brain Science, Nagoya City University Graduate School of Medical Sciences, Nagoya, Japan | [4]Division of Neural Development and Regeneration, National Institute for Physiological Sciences, Okazaki, Japan | [5]Laboratory of Comparative Neurobiology, Department of Cellular Biology, Functional Biology and Physical Anthropology, University of Valencia – CIBERNED-ISCIII, Burjassot, Spain

Correspondence: José Manuel García-Verdugo (j.manuel.garcia@uv.es) | Vicente Herranz-Pérez (vicente.herranz@uv.es)

Received: 8 April 2025 | **Revised:** 28 May 2025 | **Accepted:** 18 June 2025

Funding: This study was funded by the FEDER-EU (Grant number PID2023-151927OB-I00), AGAUR/Generalitat de Catalunya (Grant number 2021 SGR 01359), Valencian Council for Education, Universities and Employment (Grant number ACIF2021/420;CIPROM/2023/053), Core-to-Core Program of the Japan Society for the Promotion of Science (Grant number JPJSCCA20230007), Spanish Ministerio de Ciencia, Innovación y Universidades and Agencia Estatal de Investigación (Grant number MICIU/AEI/10.13039/501100011033), Grant-in-Aid for Outstanding Research Group Support in Nagoya City University (Grant number 2401101).

Keywords: adult neurogenesis | neuroblast migration | rostral migratory stream | swine brain | ventricular–subventricular zone

ABSTRACT

The ventricular–subventricular zone (V-SVZ), lining the lateral walls of the lateral ventricles, is a major neurogenic region in the adult brain of many mammals. This study investigates the structural organization and cellular composition of the V-SVZ in the juvenile swine brain (3–5 months), providing novel insights into neuroblast migration in gyrencephalic species. Using immunohistochemistry combined with transmission and scanning electron microscopy, we redefined the cytoarchitecture of the swine V-SVZ, identifying four distinct cellular layers. Layer 1 consists of a pseudostratified epithelium of glial fibrillary acidic protein-positive ependymal cells, whose cilia and microvilli extend into the ventricular lumen, frequently surrounding supraependymal axons. Beneath it, layer 2 is composed of astrocytic and radial glia processes and contains occasional clusters of doublecortin (DCX)-positive cells with prominent microtubules and elongated cytoplasm, indicative of a migratory phenotype. Layer 3 is further subdivided into a low-cell-density sublayer 3a, enriched with myelinated axons and scattered DCX$^+$ clusters, and a high-cell-density sublayer 3b, characterized by large groups of DCX$^+$ migratory cells. In sagittal sections, these cells form long chains oriented parallel to the ventricular surface. Neuroblasts emerging from the dorsal V-SVZ migrate caudorostrally through the rostral migratory stream toward the olfactory bulb. The layered organization of the swine V-SVZ resembles that of humans,

---

Abbreviations: DCX, doublecortin; DMSO, dimethyl sulfoxide; dV-SVZ, dorsal ventricular–subventricular zone; GFAP, glial fibrillary acidic protein; IHC, immunohistochemistry; laV-SVZ, lateral ventricular–subventricular zone; LV, lateral ventricle; mV-SVZ, medial ventricular–subventricular zone; NSCs, neural stem cells; OV, olfactory ventricle; PB, phosphate buffer; PFA, paraformaldehyde; RMS, rostral migratory stream; SEM, scanning electron microscopy; TEM, transmission electron microscopy; vlaV-SVZ, ventral–lateral ventricular–subventricular zone; vmV-SVZ, ventral–medial ventricular–subventricular zone; V-SVZ, ventricular–subventricular zone.

https://doi.org/10.1002/cne.70070

where DCX+ chains persist up to 18 months of age, positioning the swine as a valuable model for investigating postnatal plasticity and neurogenic potential in gyrencephalic brains. The persistence of immature neurons in the V-SVZ of gyrencephalic mammals, including infant humans, underscores the relevance of this region for neurogenesis and plasticity in large-brained species.

1 | Introduction

The ventricular–subventricular zone (V-SVZ) lines the lateral walls of the telencephalic ventricles in the adult mammalian brain. It represents one of the main neurogenic areas of the adult brain, along with the subgranular zone of the dentate gyrus of the hippocampus in many mammals (Alvarez-Buylla and García-Verdugo 2002; Kempermann et al. 2015).

The cellular components of the V-SVZ have been extensively studied in rodents and are classified into four major cell types: ependymal cells (E1 cells), astrocytes (B1 and B2 cells), transient amplifying progenitor cells (type C cells), and neuroblasts (type A cells) (Doetsch et al. 1997, Doetsch et al. 1999). Astrocytes of the V-SVZ are proliferative and are considered to be the adult neural stem cells (NSCs) in the niche (Cebrian-Silla et al. 2024). They can be further classified as B1 and B2 cells, where B1 cells contact the ventricular lumen with their primary cilium, while B2 cells lack direct contact with the lumen. B cells give rise to type C cells, transient amplifying progenitors with rapid proliferation that ultimately differentiate into neuroblasts (type A cells) (Doetsch et al. 1999).

Although it was initially characterized in rodents (Altman 1969; Doetsch et al. 1997), the cellular composition of the V-SVZ has been described in other mammalian species, such as cattle (Rodríguez-Pérez et al. 2003), sheep (Low et al. 2013), rabbits (Bonfanti and Ponti 2008; G. Ponti et al. 2006), dogs (Fernández-Flores et al. 2018), swine (Costine et al. 2015), and humans (Nogueira et al. 2014; Quiñones-Hinojosa et al. 2006; H. Sanai et al. 2004; N. Sanai et al. 2011), among others. These comparative studies have revealed notable differences in the cytoarchitecture of the V-SVZ between lissencephalic and gyrencephalic species. In the human V-SVZ, three clearly defined layers have been identified: (1) a monolayer of ependymal cells in contact with the ventricular cavity, (2) a hypocellular gap layer formed by astrocytic and ependymal cell processes and devoid of migratory cells, and (3) an astrocyte-enriched ribbon layer (Quiñones-Hinojosa et al. 2006; H. Sanai et al. 2004). In piglets (Costine et al. 2015), as well as in young dogs (Fernández-Flores et al. 2018), rabbits (G. Ponti et al. 2006), and mice, there is not a distinct hypocellular layer composed solely by glial processes, but neuroblast chains are found directly beneath the ependymal cells. In infant humans, neuroblast chains have been observed adjacent to the ependyma, declining rapidly after 6 months of age (N. Sanai et al. 2011).

In species in which olfaction is a dominant sense, such as rodents (Altman 1969), dogs (Malik et al. 2012), rabbits (G. Ponti et al. 2006), and piglets (Costine et al. 2015), neuroblasts primarily migrate from the V-SVZ toward the olfactory bulb along the rostral migratory stream (RMS). This migration contributes to the integration of new interneurons into the granular and periglomerular layers (Lois and Alvarez-Buylla 1994). In humans, while most neuronal migration occurs prior to birth, some postnatal incorporation of inhibitory interneurons into specific brain circuits persists. Immature neurons exit the V-SVZ and reach the olfactory bulb via the RMS (Paredes et al. 2016).

Moreover, in infant humans, other routes of migration originating from the V-SVZ have been observed. On one hand, young neurons in the RMS branch out ventrally into the medial migratory stream (MMS) and integrate into the ventral prefrontal cortex (N. Sanai et al. 2011). On the other hand, young neurons have been observed forming an arc-like structure (Arc) around the ventricle, from which they migrate long distances to several regions of the frontal lobe, where they integrate as interneurons (Paredes et al. 2016). In piglets, some individual neuroblast chains have been observed deviating from the RMS toward other brain regions, suggesting the existence of similar alternative migratory routes (Costine et al. 2015).

The gyrencephalic brain of the swine shares key developmental features with the human brain, such as a unique organization of doublecortin (DCX)-positive cells in the medial ganglionic eminence (MGE) that is not found in the mouse (Casalia et al. 2021). Additionally, neurogenesis and neuroblast migration patterns in the piglet V-SVZ resemble those found in infant humans (Costine et al. 2015; Porter et al. 2022), making the juvenile swine an emerging model for studying postnatal neurogenesis during later developmental stages.

Understanding the cellular organization of the juvenile swine V-SVZ is essential for establishing its potential as a model for postnatal neurogenesis in gyrencephalic species. Given the structural similarities between the swine and human V-SVZ, our study provides a framework for investigating how this neurogenic niche supports neuroblast migration and postnatal plasticity in large-brained mammals.

By redefining the layered architecture of the juvenile swine V-SVZ and detailing the spatial distribution of its cellular components, we aim to contribute to a more comprehensive understanding of the organization and function of this region. Ultimately, our findings offer a more nuanced perspective on the organization and function of this region, with potential implications for regenerative strategies and neurodevelopmental research.

2 | Materials and Methods

2.1 | Animals and Tissue Processing

Brain samples from Sus scrofa were obtained from the Center of Applied Biomedical Experimental Research (CREBA) in Lleida, Spain. The animals had been previously used in unrelated nonsurvival surgical procedures conducted under anesthesia with continuous veterinary supervision, in compliance with European Union and Spanish Government regulations (BOE-A-2013-1337). In such procedures, female pigs were preferentially used due to their more manageable temperament and the relative ease of transurethral catheterization. As a result, five of the animals included in this study were females and one was a male, all aged approximately 3–5 months. This sex distribution was not intentional but rather determined by specimen availability. The selected age range corresponds to a juvenile, postweaning, and prepubertal stage, comparable to middle childhood to early adolescence in humans, a period of active brain maturation and neuroplasticity. Animals were euthanized with a lethal dose of anesthesia, after which brains were extracted, and the hemispheres were separated and immersion -fixed.

One hemisphere from each specimen was immersion-fixed in 4% paraformaldehyde (PFA) in 0.1 M phosphate buffer (PB) for 72 h at 4°C. The contralateral hemispheres were immersion-fixed in a solution containing 2% PFA and 2.5% glutaraldehyde (GA) in 0.1 M PB for 5 days at 4°C. Following fixation, all brains were rinsed with 0.1 M PB and stored in the same buffer containing 0.05% sodium azide at 4°C. Hemispheres designated for immunohistochemistry (IHC) were cryoprotected and stored at −80°C for subsequent sectioning with a freezing microtome. Cryoprotection involved sequential immersion at 4°C in a 10% glycerol and 2% dimethyl sulfoxide (DMSO) solution in 0.1 M PB overnight, followed by immersion in a 20% glycerol and 2% DMSO solution in 0.1 M PB for 48 h. Finally, the brains were rapidly frozen by immersion in −75°C isopentane for 5 min.

2.2 | IHC

2.2.1 | Diaminobenzidine Immunostaining

Tissue fixed in 4% PFA was used for antigen detection by IHC. Free-floating 100-µm sections were obtained using a freezing microtome (Microm HM 450; Thermo Fisher Scientific). Sections were rinsed with 0.1 M PB, and antigen retrieval was performed by incubating sections for 60 min at 60°C with Immunosaver (64142; Electron Microscopy Sciences). After rinsing, sections were incubated in a solution of 3% hydrogen peroxide (H_2O_2) and 10% methanol in 0.1 M PB for 30 min to block endogenous peroxidase activity. After washing with PTA solution (0.1% Triton X-100 and 0.1% bovine serum albumin in 0.1 M PB), sections were incubated for 1 h in a blocking solution containing 10% casein and 5% normal goat serum (NGS) in PTA to prevent non-specific interactions. Primary antibodies (Table 1) were diluted in blocking solution and incubated overnight at 4°C. Following multiple washes with 0.1 M PB, sections were incubated with secondary antibodies (Table 2) in 0.3% PB-Tx in blocking solution overnight at 4°C. After additional washes with PTA, sections were incubated with the Avidin–Biotin–Peroxidase Complex (ABC; Vector Laboratories) for 1 h at room temperature in the dark and subsequently washed with 0.1 M PB. Finally, sections were incubated in a solution of 0.05% DAB and 0.003% H_2O_2 in 0.1 M PB for 10 min. After washing, sections were dehydrated in a graded ethanol series (70%, 96%, and 100%), cleared in xylene, and mounted on glass slides with Eukitt. DAB-stained samples were examined using a Nikon Eclipse E800 microscope, and images were acquired with a Nikon CCD camera.

2.2.2 | Immunofluorescence Staining

Tissue fixed in 4% PFA was embedded in paraffin following dehydration, and 10-µm sections were obtained using a microtome (MICROM HM340E). Sections were rinsed with 0.1 M PB, and endogenous peroxidases were blocked by incubating them in 3% H_2O_2 and 10% methanol in 0.1 M PB. Antigen retrieval was performed by incubating sections in Immunosaver (64142; Electron Microscopy Sciences) for 30 min at 60°C. Samples were washed with PTA and incubated for 1 h in a blocking solution containing 10% casein and 5% NGS in PTA. Primary antibodies (Table 1) were diluted in blocking solution and incubated overnight at 4°C. After washing with PTA, sections were incubated with secondary antibodies (Table 2) diluted in blocking solution for 1 h at room temperature. Sections were rinsed with 0.1 M PB and incubated for 10 min with 4′,6-diamino-2-fenilindol (DAPI; 1:1000 dilution in H_2O) to label cell nuclei. Finally, samples were mounted with FluorSave (Millipore) and examined using an Olympus FV1000 confocal microscope.

2.3 | Transmission Electron Microscopy (TEM)

2.3.1 | Sample Preparation

Coronal and sagittal sections (200-µm thick) were obtained from hemispheres fixed with 2% PFA and 2.5% GA using a Leica VT1200S vibratome (Leica Microsystems). Tissue blocks containing the region of interest were trimmed and postfixed in 2% osmium tetroxide in 0.1 M PB for 1.5 h at room temperature in the dark. Samples were rinsed with deionized water, and sequentially dehydrated in ethanol (30%, 50%, and 70%). Samples were then incubated in 2% uranyl acetate in 70% ethanol for 2.5 h at 4°C. Dehydration was continued in ethanol (70%, 96%, and 100%), followed by propylene oxide. Subsequently, tissues were embedded in Durcupan ACM epoxy resin (Fluka, Sigma–Aldrich) overnight. The following day, samples were transferred to fresh resin and polymerized at 70°C for 72 h.

2.3.2 | Semithin and Ultrathin Sectioning

After resin hardening, the samples were attached to resin blocks, and semithin sections (1.5-µm thick) were obtained with a diamond knife using an Ultracut UC7 ultramicrotome (Leica Microsystems). Sections were mounted on glass slides and stained with 1% toluidine blue. Regions of interest were identified under light microscopy. Selected semithin sections were glued with Super Glue-3 (Loctite; Henkel) onto new resin blocks and subsequently detached from the slides by freezing in liquid nitrogen. Ultrathin sections (60- to 80-µm thick) were obtained from the detached semithin sections and mounted on copper grids coated with Formvar film. For cell reconstruction, several serial ultrathin sections were obtained. Ultrathin sections were stained with lead

TABLE 1 | Primary antibodies.

Antigen	Species	Dilution	Use	Manufacturer, reference, RRID	Detection
Doublecortin, Polyclonal IgG	Rabbit	1:200	IHC, IF	Cell Signaling Technology, Cat# 4604, RRID: AB_561007	Neuroblasts
Doublecortin, Polyclonal IgG	Rabbit	1:100	IG-Au	Cell Signaling Technology, Cat# 4604, RRID: AB_561007	Neuroblasts
Doublecortin, Polyclonal IgG	Goat	1:2000	IHC, IF	Santa Cruz Biotechnology, Cat# sc-8066, RRID: AB_2088494	Neuroblasts
GFAP, Monoclonal IgG1	Mouse	1:250	IF	Millipore, Cat# MAB360, RRID: AB_11212597	Astrocytes
GFAP, Monoclonal IgG1	Mouse	1:125	IG-Au	Millipore, Cat# MAB360, RRID: AB_11212597	Astrocytes
Nestin, Polyclonal	Rabbit	1:200	IF	Sigma–Aldrich Cat# N5413, RRID: AB_1841032	Epithelial stem cells
Ki67, Monoclonal IgG1	Rabbit	1:200	IF	Abcam Cat# ab16667, RRID: AB_302459	Proliferating cells
Ki67, Monoclonal IgG	Rat	1:100	IF	Invitrogen, Cat# 14-5698-82, RRID: AB_10854564	Proliferating cells

TABLE 2 | Secondary antibodies.

Antibody	Species	Dilution	Use	Manufacturer, reference, RRID
Anti-rabbit (H+L) Alexa 555	Goat	1:300	IF	Molecular Probes, Cat# A-21428, RRID: AB_141784
Anti-rabbit biotinylated	Goat	1:300	IHC	Vector Laboratories, Cat# BA-1000, RRID: AB_2313606
Anti-rabbit gold 10 nm	Goat	1:50	IG-Au	Sigma–Aldrich, Cat# G7402, RRID: AB_259953
Anti-mouse Alexa 488	Goat	1:300	IF	Molecular Probes, Cat# A-21424, RRID: AB_141780
Anti-mouse gold 10 nm	Goat	1:50	IG-Au	Sigma–Aldrich, Cat# G7652, RRID: AB_259958
Anti-goat biotinylated IgG (H+L)	Rabbit	1:200	IHC	Vector Laboratories, Cat# BA-5000, RRID: AB_2336126
Anti-goat IgG (H+L) Alexa 488	Donkey	1:500	IF	Jackson ImmunoResearch, Cat# 705-546-147, RRID: AB_2340430
Anti-rat IgG (H+L) Alexa 405	Goat	1:250	IF	Invitrogen, Cat# A48261; RRID: AB_2890550

citrate (Reynolds' solution) for 10 min and examined with an FEI Tecnai G^2 Spirit transmission electron microscope at 80 kV (FEI Europe). Images were acquired using a XAROSA CMOS digital camera (EMSIS GmbH).

2.4 | Immuno-Gold Staining

Free-floating 50-µm coronal sections were obtained from hemispheres fixed in 4% PFA using a Leica VT1200S vibratome (Leica Microsystems). Sections were cryoprotected in 25% sucrose in 0.1 M PB for 30 min, followed by permeabilization through freeze–thaw cycles in methyl butane at −60°C. After rinsing in 0.1 M PB, sections were incubated for 1 h at room temperature in blocking solution (0.3% bovine serum albumin C [BSAc] and 0.05% sodium azide in 0.1 M PB). Primary antibodies (Table 1) were diluted in blocking solution and incubated for 96 h at 4°C. After washes with 0.1 M PB, sections were blocked with a secondary blocking solution (0.5% BSAc and 0.1% fish gelatin in 0.1 M PB) for 1 h.

Sections were then incubated with colloidal gold-conjugated secondary antibodies (0.8 nm; Aurion) (Table 2) for 24 h at 4°C. Samples were washed with 0.1 M PB, rinsed in 2% sodium acetate in distilled water, and subjected to silver enhancement using a commercial Silver Enhancement kit (Aurion) to intensify the immunogold signal. Subsequently, samples were washed again in 2% sodium acetate. To stabilize the silver particles, sections were treated with 0.05% gold chloride in distilled water for 10 min at 4°C. Afterward, samples were rinsed in 0.03% sodium thiosulfate and 0.1 M PB. Finally, samples were postfixed in 2% GA for 30 min and thoroughly washed in 0.1 M PB. Sections were contrasted with 1% osmium tetroxide and 7% glucose in 0.1 M PB for 30 min. Dehydration, resin embedding, semithin and ultrathin sectioning, and image acquisition followed the procedures described in Section 2.3.

2.5 | Scanning Electron Microscopy (SEM)

A fragment containing the V-SVZ was dissected from a brain fixed with 2% PFA and 2.5% GA, then washed in 0.1 M PB. The tissue was then immersed in a 2% osmium tetroxide solution for 1–2 h. After rinsing with distilled water, the sample was dehydrated through a graded ethanol series (30%, 50%, 96%, and 100%), followed by critical point drying with CO_2. The dried samples were coated with a gold/palladium alloy using a sputter coater. The surface of the lateral wall was examined using a Hitachi S-4800 scanning electron microscope, and images were acquired with Quantax 400 software (Bruker).

3 | Results

3.1 | General Morphological Features of the Swine V-SVZ

To perform an in-depth characterization of the area covered by the V-SVZ, the swine brain was coronally sectioned into four rostrocaudal levels. Following the nomenclature previously established by several authors (Porter et al. 2022), these levels are referred to as anterior end (AE), anterior (A), middle (M), and posterior (P) (Figure 1A–D). Furthermore, at each of these levels, the V-SVZ was subdivided into five distinct regions, based on their anatomical position: (1) the dorsal area (dV-SVZ), which borders the corpus callosum dorsally; (2) the medial walls of the ventricle (mV-SVZ), adjacent to the cingulate cortex (Cg Cx); (3) the lateral walls of the ventricle (laV-SVZ), adjacent to the caudate nucleus; (4) the ventral–medial V-SVZ (vmV-SVZ), next to the nucleus accumbens at anterior-end level; and (5) the ventral–lateral V-SVZ (vlaV-SVZ), associated with the piriform lobe at anterior, medial, and posterior levels, corresponding to the opening of the inferior horn of the ventricle.

To investigate potential differences in the structural organization of the V-SVZ across the four rostrocaudal levels, we combined DAB-based IHC and immunofluorescence with electron microscopy techniques. Our results revealed a widespread expression of DCX throughout the entire V-SVZ, with some notable regional variations. Generally, we identified four cellular layers based on DCX expression: the ependymal layer (layer 1), negative for DCX; the subependymal layer (layer 2), with occasional clusters of DCX^+ cells; and two myelinic layers (Sublayers 3a and 3b), with either small or large DCX^+ clusters (Figure 1E).

The swine dV-SVZ, located above the striatum, shows an arc-like structure (Figure 1Ai,Bi,Ci,Di), in which we clearly observe this layered organization. Layer 1, which is in direct contact with the ventricular lumen, corresponds to a monolayer of ependymal cells that coats all the ventricle's surface. The subependymal layer (layer 2) is located immediately beneath the ependyma and is composed of clusters of DCX^+ cells (Figure 1F). The innermost region of the dV-SVZ corresponds to an abventricular area (A-SVZ) containing DCX^+ cells. Within this area, sublayer 3a (Figure 1G) is defined by the presence of scarce and small clusters of DCX^+ cells, whereas sublayer 3b corresponds to the most dorsal region, which harbors large clusters of DCX^+ cells closely associated with prominent blood vessels (Figure 1H).

At the laV-SVZ (Figure 1Aii), mV-SVZ (Figure 1Bii,Cii), vmV-SVZ (Figure 1Aiii), and vlaV-SVZ (Figure 1Biii,Ciii,Diii), some of these four layers become less defined. Due to the narrowing of the V-SVZ, sublayers 3a and 3b are not distinguishable in these regions. While layer 1 is maintained, layer 2 DCX expression varies in each region. The laV-SVZ only shows DCX^+ cells at anterior-end levels, while no clusters are observed in anterior, medial, and posterior levels. The layer 2 of the mV-SVZ is formed by an almost continuous layer of DCX^+ cells in all rostrocaudal levels (Figure 1Aii,Bii,Cii,Dii). Occasionally, some isolated DCX^+ cells are seen migrating outside of the mV-SVZ toward the white matter (Figure 1Aii,Dii). Layer 2 at vmV-SVZ (Figure 1Aiii) becomes a disorganized network of DCX^+ cells that extends into the white matter. At vlaV-SVZ, layer 2 is also diffuse, but DCX^+ cells migrating into the white matter aggregate into more organized clusters (Figure 1Biii,Ciii,Diii).

Since the layer organization of the V-SVZ was clearer at dorsal (arc) levels, the detailed descriptions in the following sections mostly refer to the dorsal V-SVZ.

3.2 | Ependymal Cells Lining the V-SVZ Walls Form a Monolayer and Interact With Supraependymal Axons

The ultrastructural characteristics of the cellular layers forming the V-SVZ were analyzed by means of IHC and electron microscopy techniques. Layer 1 of the V-SVZ consists majorly of cuboidal multiciliated ependymal cells (Figure 2A). They form a one-cell-thick epithelium with strong junctional complexes and pronounced interdigitations. The nuclei of these cells are elongated and located in the basal portion of the cell body. They display small invaginations and clumped chromatin (Figure 2B).

At the organelle level, these ependymal cells contain numerous dictyosomes with well-developed saccules, though the rough endoplasmic reticulum is scarce and does not form parallel stacks of cisternae. There is also a high density of mitochondria, predominantly in the apical region. Ciliary basal bodies are typically anchored by ciliary rootlets to mitochondria, though occasionally they can occasionally attach to the nuclear surface. These cells extend long radial processes enriched in intermediate filaments (Figure 2D), which contribute to the composition of layer 2.

Most of the observed ependymal cells are densely covered with cilia distributed across their apical surface, with their highest concentration at the central region (Figure 2E). Basal bodies are positioned in the apical region of the cell, displaying structural variability. Basal bodies with simpler arrangements (Figure 2F) correspond to multiciliated cells. However, we found more complex structures with elaborate raceme-like appendages, possibly associated with biciliated cells (Figure 2G). We also observed rarely uniciliated cells in serial sections (Figure 2H).

Furthermore, unmyelinated axons (Figure 2I), filled with various types of vesicles, either clear or electron-dense, were observed on the surface of these cells. These axons are closely associated with the ependymal surface, which extends numerous microvilli over them (Figure 2I,J). In some cases, these axons form adherens

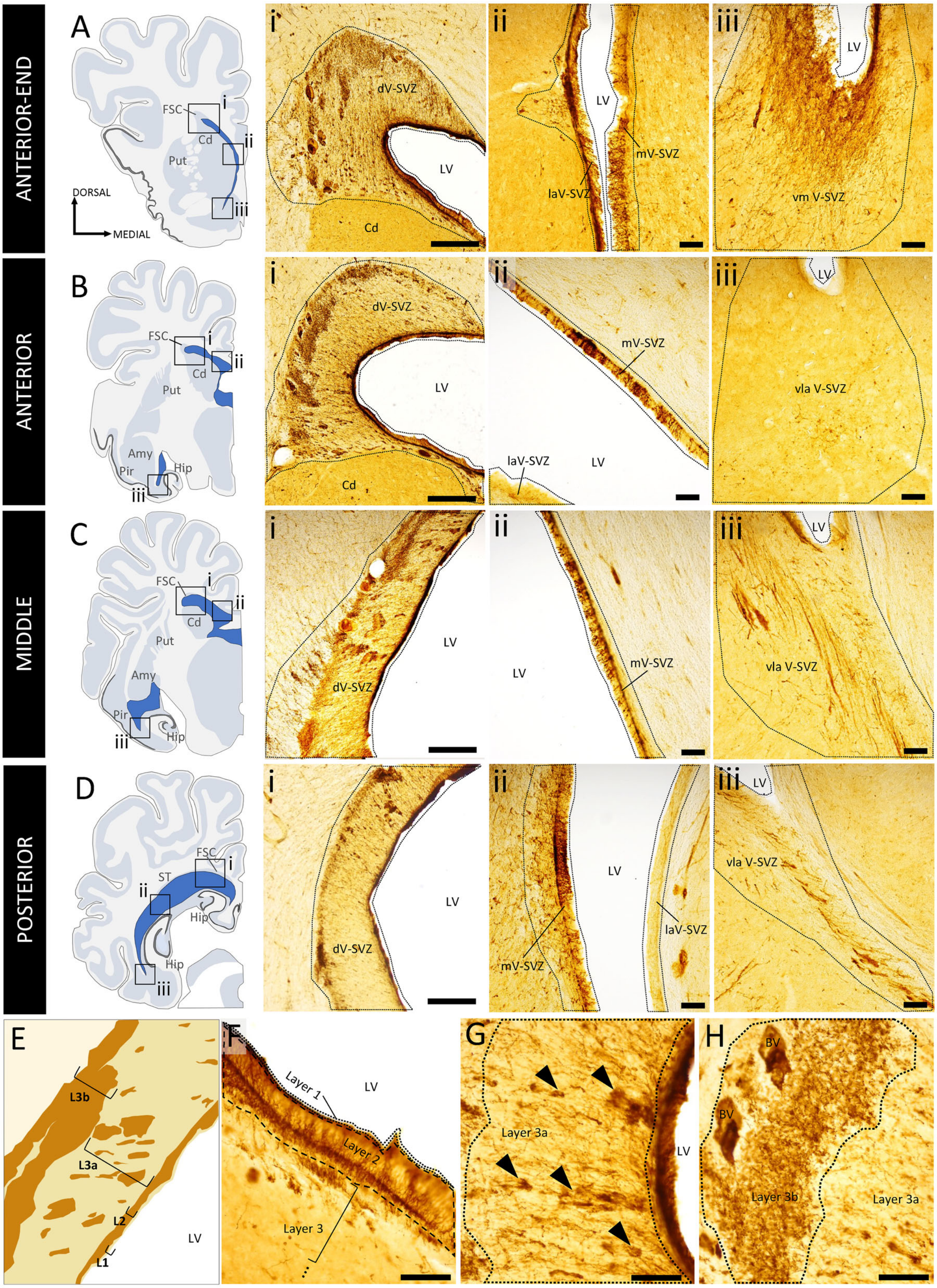

FIGURE 1 | Organization of the swine V-SVZ based on DCX expression. (A–D) Schematic representation of four rostrocaudal levels (anterior-end [AE], anterior [A], middle [M], and posterior [P]) in coronal sections of the juvenile swine brain (3–5 months old). Squares indicate representative regions of the V-SVZ stained by DAB immunohistochemistry for DCX in 100-µm-thick coronal sections. (i) Dorsal V-SVZ: characterized by large DCX$^+$ clusters located at the innermost region of the arc. These chains are more abundant at AE and A levels, gradually decreasing at M and P levels. (ii) Lateral (subpallial, striatal) and medial (Cg Cx) V-SVZ: maintain a consistent rostrocaudal organization, appearing as a thin layer of DCX$^+$ cells lining the ventricle wall, with occasional small clusters. The medial V-SVZ (Cg Cx) is shown at AE, A, and M levels (Aii, Bii, Cii), while the lateral V-SVZ (striatal) is only shown at AE level (Aii). (Aiii) Ventral–medial V-SVZ: at the AE level, it corresponds to the ventral region of the anterior horn, displaying a mesh-like network of DCX$^+$ cells. (Biii, Ciii, Diii) Ventral–lateral V-SVZ (piriform lobe). At A, M, and P levels, it corresponds to the posterior horn of the

lateral ventricle, where DCX$^+$ cell chains are most prominent at M level. (E) Schematic representation of DCX$^+$ cell distribution, highlighting a layered organization. (F) Layer 1 adjacent to the ventricular lumen, devoid of DCX labeling, and layer 2 enriched in DCX$^+$ chains. (G) Layer 3a characterized by small DCX$^+$ clusters (arrowheads). (H) Layer 3b is composed of large groupings of DCX$^+$ cells adjacent to blood vessels. Scale bar: 500 µm for dorsal column images; 100 µm for all other images. FSC, fasciculus subcallosus; Put, putamen; Amy, amygdala; Cd, caudate; Hip; hippocampus; Pir, Piriform cortex; ST, stria terminalis.

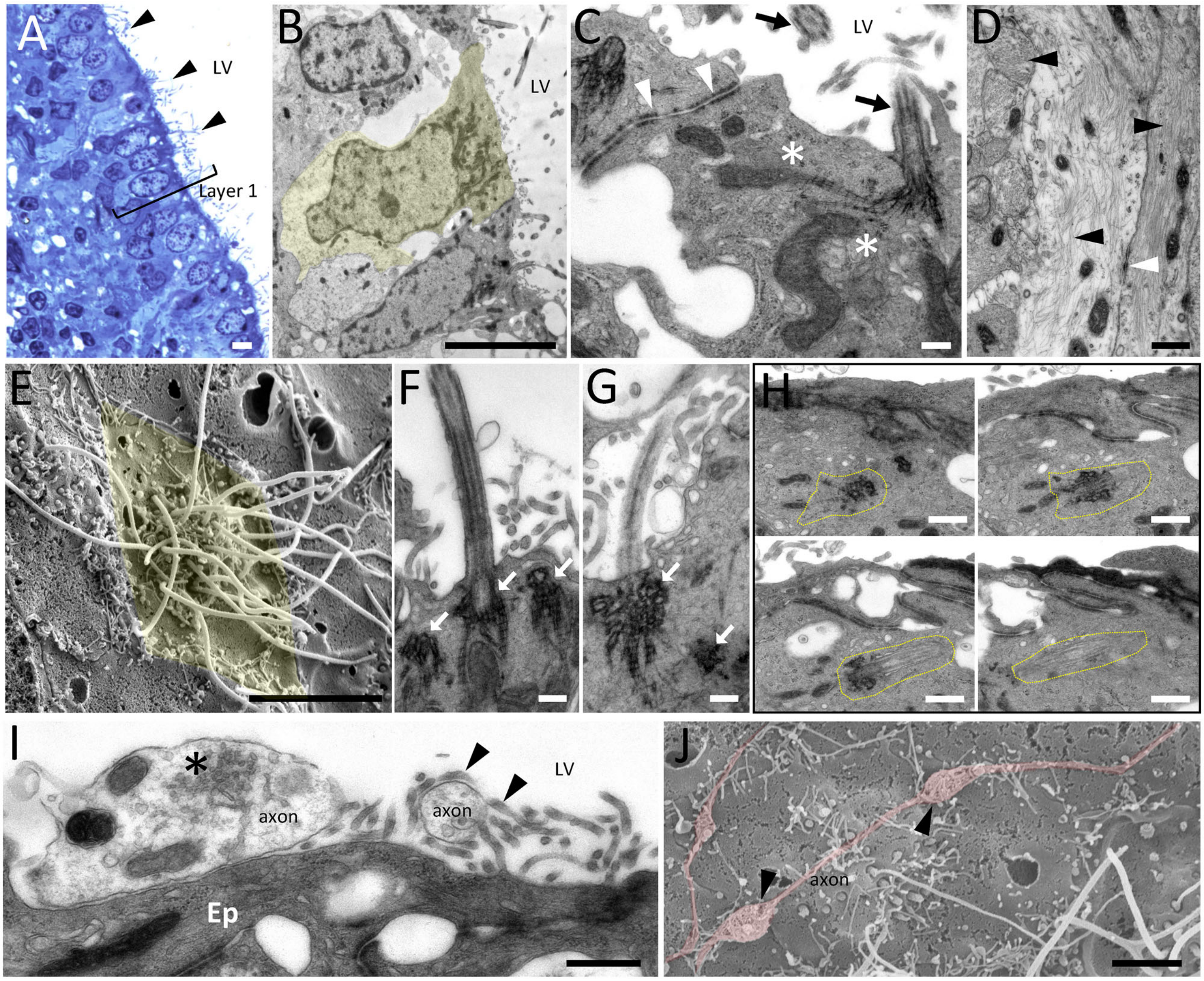

FIGURE 2 | Ultrastructure of the ependymal layer. (A) Semithin section stained with toluidine blue showing the typical organization of the swine ependymal layer forming a pseudostratified epithelium. (B) Ependymal cells localize most of their organelles to the basal region of the cytoplasm. (C) Ependymal cells establish strong dense junctions (white arrowhead) between them and display multiple cilia (black arrows), which are anchored to mitochondria (asterisks) by ciliary rootlets. (D) The basal region contains processes enriched in intermediate filaments (black arrowheads) that project into layer 2. These cell processes also make dense junctions between them (white arrowhead). (E) SEM image of a multiciliated ependymal cell, with cilia concentrated in the central region of the apical surface. (F, G) Basal body complexes (arrows) from a multiciliated cell (F) and a biciliated cell (G). (H) Three-dimensional reconstruction of the basal body complex in a uniciliated cell. (I) Supraependymal axons in the ventricular lumen establish contact with ependymal cells. These axons contain both electron-dense and clear vesicles (asterisk) and are surrounded by microvilli (arrowheads). (J) SEM image of supraependymal axons (arrowheads) encased by microvilli. Scale bars: 5 µm (A, B, E); 2 µm (J); 200 nm (C, F, G); and 500 nm (D, H, I).

junctions with the ependymal surface; however, no typical synaptic contacts were observed. When analyzing the ventricular surface with SEM, these axons appeared as thin, elongated filaments with spherical thickenings, measuring approximately 600 nm in diameter (SD ±346.21 nm; $n = 30$).

3.3 | Subependymal Layer 2 Is Composed of Glial Expansions and Neuroblast Chains

The layer immediately below the ependyma, identified as subependymal or layer 2 (Figure 3A), consists primarily of

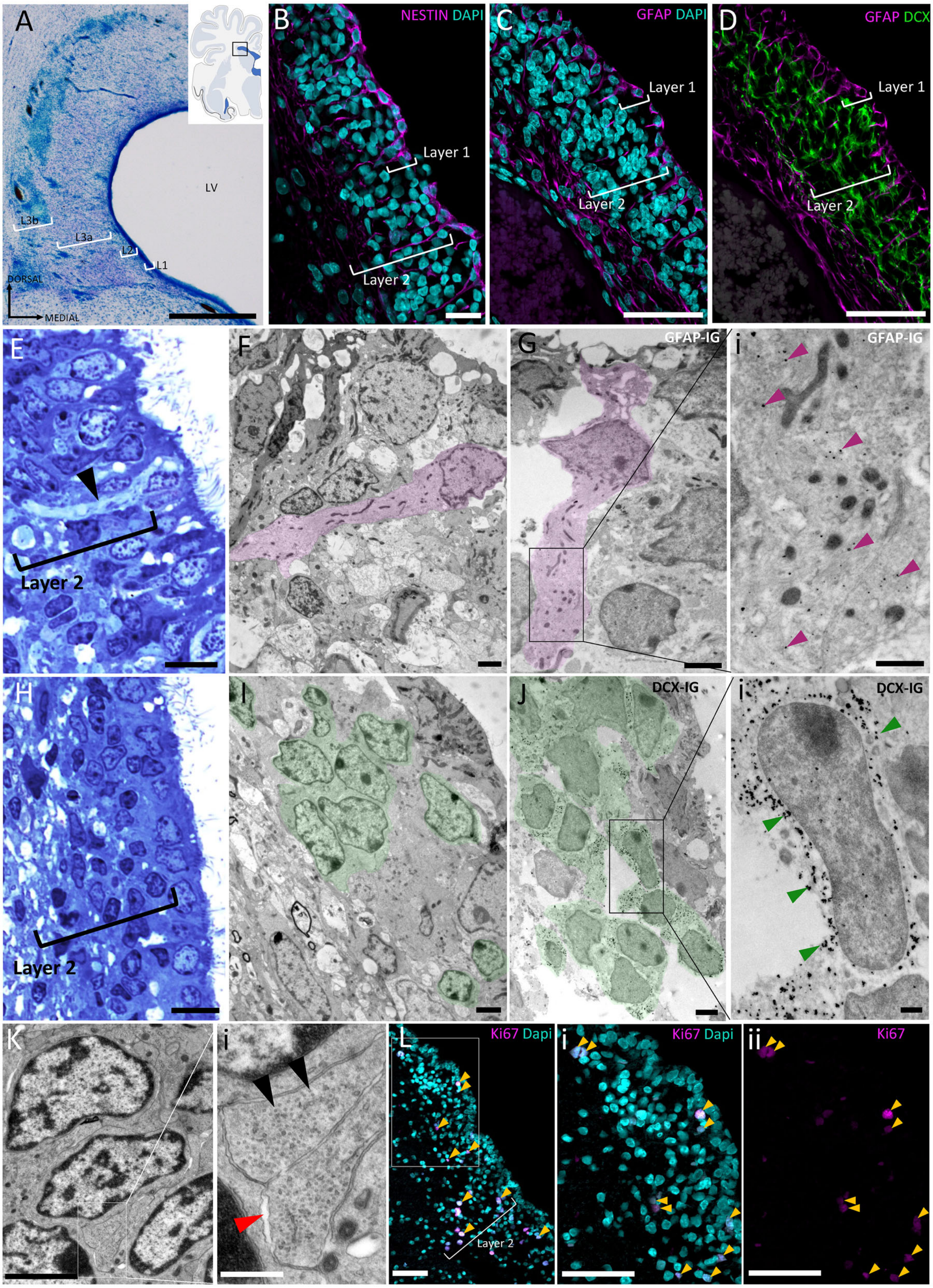

FIGURE 3 | Cellular composition of layer 2 of the dorsal V-SVZ. (A) Nissl-stained coronal section showing the layered structure of the dorsal V-SVZ. (B–D) Immunostaining in the dV-SVZ. Layer 1 is positive for Nestin and GFAP, while layer 2 is labeled by DCX. (E, H) Semithin sections stained with toluidine blue. (F, G, Gi, I, J, Ji, K, Ki) TEM micrographs. (E) Ependymal cell processes (arrowhead) in layer 1 extend into layer 2. (F) These processes exhibit clear cytoplasm containing numerous mitochondria and intermediate filaments. Immunogold labeling for GFAP (G, Gi) labels these intermediate filaments (arrowheads). Small cell clusters are present in layer 2 (H). Ultrastructurally, these cells display migratory-like features (I). Immunogold staining (arrowheads) confirms DCX expression in these cells (J, Ji). Their chromatin forms clumps along the inner nuclear envelope (K), reduced cytoplasm with few organelles, and microtubules in their cell processes (black arrowheads). Intercellular spaces are occasionally observed (red arrowhead). (L, Li) Ki-67 immunostaining reveals proliferating cells in both layers (1 and 2). Scale bars: 500 µm (A); 20 µm (B, C, D); 10 µm (E, H); 2 µm (F, G, I, J, M); 500 nm (Gi, Ji, Mi); and 50 µm (O, Oi, Oii).

ependymal expansions from layer 1, astrocytic processes from layer 3, and clusters of migratory-like cells. As it can be observed with immunofluorescence, ependymal and astrocytic processes are labeled with neuroepithelial stem cell protein (Nestin) (Figure 3B) and glial fibrillary acidic protein (GFAP) (Figure 3C), while clusters of neuroblasts stain for DCX (Figure 3D).

Ependymal and astrocytic processes (Figure 3E) are readily identifiable by TEM due to the presence of intermediate filaments (Figure 3F), which was confirmed by immunogold pre-embedding for GFAP (Figure 3G). Adherens junctions are commonly observed between these processes, and the density of these filaments is variable between expansions.

Besides astrocytic expansions, astrocytic cell bodies were also found in layer 2. They exhibit an irregular nucleus, sometimes with invaginations, and chromatin arranged in clumps. Their cytoplasmic matrix is relatively electron-lucent and contains few organelles, including mitochondria. Their cytoplasmic contour is highly irregular, and intermediate filaments are distributed throughout the cell, including the cell body. They establish adherens junctions with neuroblasts and with other structures, and some of the cell processes can also make direct contact with blood vessels. Additionally, this layer contains bundles of unmyelinated axons.

Moreover, our interest was focused on the migratory chains of neuroblasts that are widely distributed across layer 2 (Figure 3H) and vary their arrangement along the rostrocaudal axis. These chains consist of multiple migratory cells surrounded almost completely by ependymal and astrocytic processes (Figure 3I). Migratory cells have a slightly irregular nucleus without invaginations, with chromatin primarily condensed near the nuclear membrane. Their cytoplasm is sparse, containing very short and dilated rough endoplasmic reticulum, small Golgi apparatus, small mitochondria, a high density of polyribosomes, and microtubules (Figure 3K).

Immunogold labeling for DCX (Figure 3J) facilitates the identification of cells within migratory chains and their associated cell processes. These expansions contain large arrays of microtubules interspersed with small reticulum cisternae and mitochondria. Their contours are smooth, and they form adherens junctions with other cellular processes, irrespective of whether they contain microtubules or intermediate filaments. While some migratory cells exhibit intercellular spaces, this is an uncommon feature.

Notably, layer 2 presented Ki-67 expression (Figure 3L), suggesting ongoing cellular proliferation in this region at this developmental stage.

3.4 | Neuroblast Chains in Layer 3 Are Organized Into Small and Large Cell Groups and Are Surrounded by Astrocytes

Layer 2 transitions to layer 3 with a sharp decline in neuroblast chains, giving way to a parenchyma-like area filled with astrocytic expansions and both myelinated and unmyelinated axons (Figure 4A). Based on cellular density, layer 3 can be further subdivided into two layers. Sublayer 3a, adjacent to layer 2, exhibits lower cellular density and contains small, scattered clusters of DCX$^+$ cells (Figure 4B). Sublayer 3b, the region further toward the ventricle's lumen, is characterized by large groups of DCX$^+$ cells located dorsally and bordering the white matter from the corpus callosum (Figure 4B). These clusters are surrounded by a meshwork of GFAP$^+$ astrocytes, which also intermingle within the cell groups (Figure 4Bi,ii).

Cell aggregates in sublayer 3a (Figure 4C) are small, averaging 10–12 cells per aggregate, and in serial coronal sections, these clusters do not form long continuous chains but appear to be oval or spherical in shape. They are surrounded almost entirely by cell processes with intermediate filaments (Figure 4D). These cell processes originate from either mature star-shaped astrocytes from layer 3 or even radial glia processes from layer 1. Expansions containing microtubules correspond to migratory neurons (Figure 4E). They display junctions between their somas (Figure 4F), and intercellular spaces are not visible in this sublayer 3a. Expansions with microtubules exhibit a more regular shape and form junctions with each other and with the intermediate filament-containing processes (Figure 4G).

Cell clusters in sublayer 3b (Figure 4H) consist of large aggregations of cells and are typically found adjacent to blood vessels. The cells within these clusters are ultrastructurally similar to those in sublayer 3a, exhibiting irregular nuclei with clumped chromatin and reduced cytoplasm containing few organelles (Figure 4I,J). Intercellular spaces are more frequently observed in sublayer 3b cells than in sublayer 3a cells (Figure 4K). Also, due to the high prevalence of amyelinic and myelinic axons in this layer, both types could be observed intermingled within the large cell clusters of sublayer 3b.

Regarding other cell types, neuronal cell bodies were not observed in either sublayer, as confirmed by the lack of NeuN marker expression. Astrocyte bodies were frequently found in both sublayers 3a and 3b and show the typical ultrastructure of mature star-shaped astrocytes, with an electron-lucent cytoplasm, long and thin endoplasmic reticulum cisternae, and expansions filled with intermediate filaments.

Oligodendrocytes, consistent with the high density of myelinated axons in this region, are also abundant in layer 3. These cells, with a wavy contour that adapts to adjacent structures, are characterized by round nuclei with clumped chromatin, short and dilated rough endoplasmic reticulum, and an electron-dense cytoplasm rich in free ribosomes—ultrastructural features characteristic of oligodendrocytes.

Immunogold labeling for DCX (Figure 4L,Li) confirmed the presence of neuroblasts within the clusters, while GFAP-gold labeling highlighted astrocytic processes surrounding them (Figure 4M,Mi). Additionally, Ki-67 immunofluorescence staining (Figure 4N,Ni) revealed a relatively uniform distribution of proliferating cells across layer 3, with cells present both within the clusters and in regions lacking them.

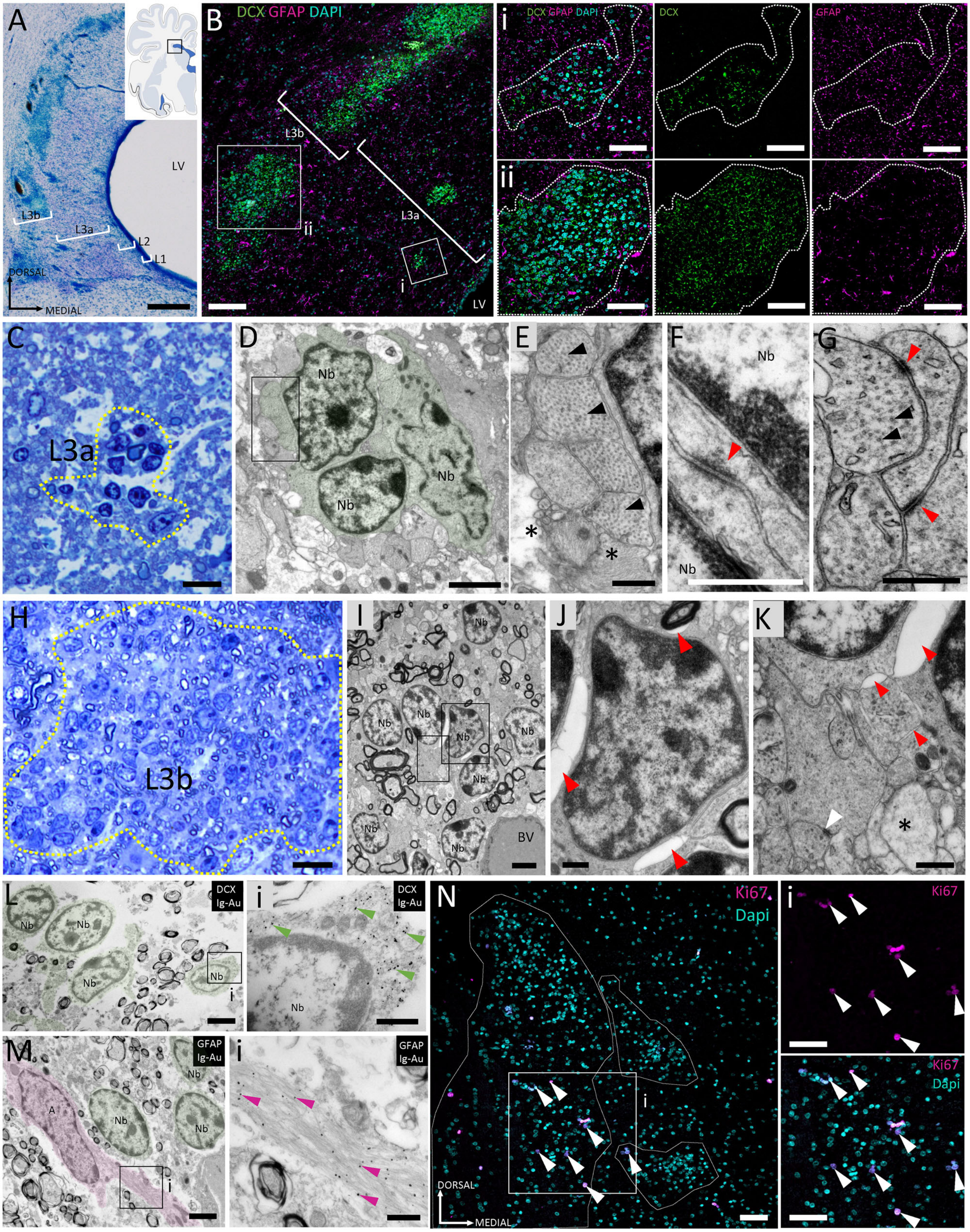

FIGURE 4 | Distribution of neuroblast chains in V-SVZ layer 3. (A) Nissl-staining on a coronal section of the dV-SVZ, indicating the cellular layers. (B) Double immunostaining for DCX and GFAP reveals that sublayer 3a contains small DCX$^+$ clusters, whereas sublayer 3b harbors larger DCX$^+$ groupings. (i) Higher magnification view of a small DCX$^+$ cluster in layer 3a. (ii) Higher-magnification view of a large DCX$^+$ cluster in sublayer 3b. GFAP$^+$ astrocytes not only surround the cluster but also extend their processes between DCX$^+$ cells. (C, H) Semithin sections stained with toluidine blue showing small and large cluster in sublayers 3a and 3b, respectively. (D–G, I–K) TEM micrographs from ultrathin sections. (D) A small cluster of migratory-like cells displaying clumped chromatin, a slightly irregular nucleus, and a reduced cytoplasm with few organelles. (E) These cells extend processes rich

in microtubules (black arrowheads), which are ensheathed by astrocytic cytoplasmic expansions containing intermediate filaments (asterisks). (F, G) Migratory cells establish frequent dense contacts (red arrowheads) both at their soma (F) and between their processes (G). (I) A large cluster of migratory cells. (J, K) Migratory cells in layer 3b also form adherens junctions (white arrowhead), but intercellular spaces (red arrowheads) are more frequently observed. These large clusters are likewise surrounded by astrocytic processes containing intermediate filaments (asterisk). (L, M) Pre-embedding immunogold labeling highlights DCX$^+$ migratory cells (Li) and GFAP$^+$ astrocytic processes enveloping the clusters (Mi). (N) Immunostaining reveals dividing cells in both sublayers; however, proliferation does not specifically correlate with the presence of clusters (Ni). Scale bars: 250 μm (A, B); 50 μm (Bi, Bii, N, Ni); 10 μm (C, H); 2 μm (D, I, L, M); and 500 nm (E, F, G, J, K, Li, Mi).

3.5 | Neuroblast Clusters From Sublayers 3a and 3b Converge During Migration Through the RMS

After analyzing the structural organization of the swine V-SVZ, we questioned whether this layered arrangement is related to neuroblast migration, potentially delineating distinct migratory routes (Figure 5A). The olfactory ventricle (OV) in the juvenile swine is continuous with the lateral ventricle (LV). Because of this, our hypothesis is that layer 2 is conserved along all the extension of the ventricle's wall, with DCX$^+$ neuroblast clusters being more frequent rostrally and scarcer caudally, while layer 3 neuroblasts would be the ones migrating toward rostral areas.

Interestingly, DAB immunostaining for DCX revealed that, within the arc-like structure of the V-SVZ, small clusters in sublayer 3a are not entirely spherical but elongated and oriented rostrally (Figure 5Bi). Furthermore, they seem to be exiting sublayer 3a and moving toward the larger clusters in sublayer 3b (Figure 5Bii), blurring the limits between layer 3a and layer 3b.

To trace the trajectory of layer 3 DCX$^+$ chains, we analyzed serial sagittal sections by immunofluorescence for DCX and GFAP (Figure 5C). At more lateral levels, DCX$^+$ clusters appear as small independent groups and even individual DCX$^+$ cells with elongated bodies (Figure 5Ci). At medial levels, small and large DCX$^+$ chains from sublayers 3a and 3b progressively merge (Figure 5Ci) into a single large group of migrating cells (Figure 5Ciii), leading the region of migration.

3.6 | Neuroblasts Migrate Through the RMS Reaching the OB, but Also Other Cortical Regions

After confirming that DCX$^+$ clusters from the V-SVZ follow the RMS, the next step was to determine their destination. To assess whether they reached the olfactory bulb, DAB IHC was performed on horizontal sections (Figure 6A). This approach allowed simultaneous visualization of both the LV and OV, revealing DCX$^+$ chains in the region connecting the two structures (Figure 6Ai). Interestingly, some neuroblast chains exiting the V-SVZ exhibited proliferative activity, as indicated by Ki-67 immunofluorescence (Figure 6Bi,ii).

To investigate whether the chains near the OV share similarities with those originating from the V-SVZ, adjacent regions were examined in sagittal sections. DCX$^+$ cell chains were observed in proximity to the ventricle (Figure 6C). Interestingly, while some chains reached the OV, another population of DCX$^+$ cells appeared to deviate from the V-SVZ toward the anterior olfactory area (Figure 6Di), suggesting the existence of additional migration pathways targeting different brain regions.

3.7 | The Layered Organization of the V-SVZ Becomes Diffused Through the RMS and Is Not Found in the OB

As expected, neuroblasts exiting the V-SVZ (Figure 7A) displayed ultrastructural features characteristic of migratory neurons. Whether located within migratory chains in layer 3 (Figure 7Ai,ii) or closer to the ventricle in layer 2 (Figure 7Aiii), these cells exhibited clumped chromatin and a small cytoplasm volume with scarce organelles. Their cytoplasmic processes were rich in microtubules, and intercellular spaces were frequently observed between them (Figure 7B,C), reinforcing the idea that they are actively migrating.

In contrast, the ultrastructure of cells at the opening of the OV revealed a different organization (Figure 7D,Di). Rather than forming distinct layers, neuroblasts were interspersed within a mesh of astrocytic processes (Figure 7E). Morphologically, these neuroblast clusters resembled those in layer 2 of the V-SVZ, consisting of small groups of immature neurons (Figure 7F) with clumped chromatin, a reduced cytoplasmic volume, and microtubule-rich processes that contacted astrocytic expansions containing intermediate filaments (Figure 7G). However, unlike migratory chains in the RMS, these clusters exhibited fewer intercellular spaces and more frequent adherens junctions between neuroblasts (Figure 7H), suggesting a different mode of organization.

4 | Discussion

The primary aim of this study was to analyze the structural organization and cellular features of the V-SVZ in the brain of 3- to 5-month-old juvenile swine. This developmental stage provides a valuable translational model for investigating neurodevelopmental processes and disorders that emerge during adolescence, a critical window of vulnerability in humans (Giedd et al. 2008). The study included five female and one male juvenile swine, a sex distribution that was not intentional but rather determined by specimen availability. While this imbalance limits the assessment of potential sex-related differences, the findings in the single male were consistent with those observed in females, supporting the overall interpretation. Nevertheless, future studies should aim to address possible sex-dependent variation in the V-SVZ.

Using IHC, we identified the main cell types composing the V-SVZ based on molecular marker expression. Additionally, electron microscopy allowed us to examine the ultrastructural characteristics of ependymal cells and neuroblast clusters in the region. Furthermore, we described the distribution of these clusters along the RMS toward the olfactory bulb, observing similar cellular characteristics and distinct migration pathways.

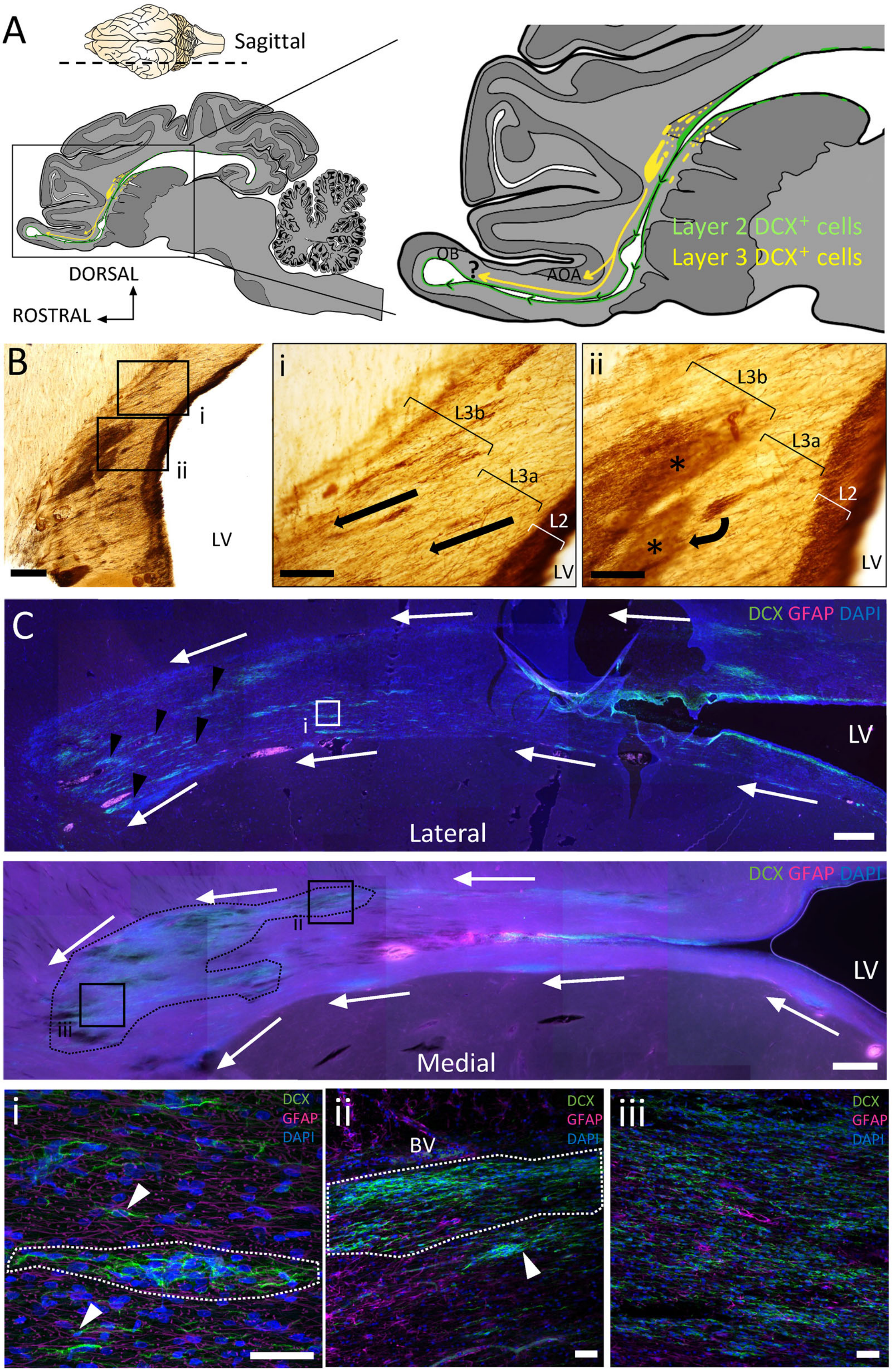

FIGURE 5 | Chain migration through the rostral migratory stream. (A) Sagittal sections (100-µm thick) were used to study the migratory path of the chains emanating from the V-SVZ. A schematic representation illustrates the direction of neuroblast migration. DCX$^+$ cells in layer 2 (green) are always found close to the ventricle's wall, either at the lateral ventricle or the olfactory ventricle. They migrate rostrally through the RMS (green arrows). DCX$^+$ cells in layer 3 (yellow) exit the V-SVZ and are directed toward frontal areas of the brain (yellow arrows), like the anterior olfactory area (AOA) or the olfactory bulb (OB), for example. (B) DAB immunostaining for DCX reveals that chains in sublayer 3a are oriented rostrally (Bi, arrows) and progressively migrate toward layer 3b and group (Bii, arrow) to form larger chains (Bii, asterisks). (C) Immunofluorescence for DCX and GFAP, at two sagittal levels (lateral and medial), shows how DCX$^+$ chains (green) migrate rostrally out of the V-SVZ. Moreover, in lateral levels (top), clusters are smaller and more scattered at the leading front of the migration (arrowheads), whereas in medial sections (bottom), neuroblast chains coalesce into a

single large cluster (dotted line). At higher magnification, we observe the small DCX$^+$ clusters (i, dotted line) surrounded by GFAP$^+$ processes (magenta) and even individual DCX$^+$ cells (i, arrowhead). In medial levels, we appreciate how smaller clusters (ii, arrowhead) become closer to large groups (ii, dotted line) and they become one large mass of DCX$^+$ cells in which GFAP$^+$ processes are less frequent (iii). Scale bars: 100 μm (B, Bi, Bii); 500 μm (C); and 50 μm (Ci, ii, iii).

The V-SVZ is the region adjacent to the LV walls, and previous studies have analyzed its organization in piglets up to 4 months of age (Costine et al. 2015; Porter et al. 2022). These authors described two distinct areas within the V-SVZ based on localization and cellular organization: the ventricular and the abventricular regions. Consistent with these findings, our DAB immunostaining revealed that, in the juvenile swine brain, the ventricular region consists of a first ependymal cell layer lining the ventricle and an adjacent layer of DCX$^+$ cell clusters (layer 2), which extend along the medial wall of the ventricle but are absent from the lateral wall over the caudate nucleus.

The abventricular region, which extends dorsolaterally in an arc-like shape, is mainly composed of astrocytic parenchyma and amyelinic and myelinic axons. Moreover, it also contains dispersed small DCX$^+$ clusters, while larger DCX$^+$ cell collections are found at the dorsal boundary, closely associated with large blood vessels. Based on these results, we established four cellular layers within the swine V-SVZ: the ventricular area was subdivided into layer 1 (ependyma) and layer 2 (subependymal), while the abventricular area was subdivided into sublayer 3a (low cellular density) and sublayer 3b (high cellular density).

Layer 1 (ependyma) consists of a pseudostratified epithelium of GFAP$^+$ Nestin$^+$ cuboidal cells, most of which are multiciliated, with cilia concentrated at the center of the apical surface. These cells correspond to E1-type ependymal cells, which may play a role in cerebrospinal fluid (CSF) circulation, as observed in mice (Mirzadeh et al. 2017; Sawamoto et al. 2011). Uniciliated cells, which are considered NSCs in mice, were rarely observed at the early ages studied. In humans, GFAP$^+$ cells have been reported in contact with the ventricular lumen, but their possession of primary cilia remains unclear (N. Sanai et al. 2011).

Electron microscopy and SEM revealed the presence of supraependymal axons in close contact with ependymal cells and surrounded by their microvilli. In mice, these axons have been identified as serotonergic axons from the raphe nuclei, which form a network over the ventricular wall, contacting both E1 and B1 cells and playing a role in NSC regulation. Similar supraependymal axons have been observed in humans, where they exhibit both clear and dense vesicles as well as bouton-like enlargements (Tong et al. 2014). However, in swine, their origin and neurotransmitter identity remain undetermined.

Layer 2 (subependymal layer) is composed primarily of cellular processes from ependymal cells and astrocytes, both rich in intermediate filaments and immunoreactive for Nestin and GFAP. Although previous studies report a rapid decline in radial glial cells in swine with age (Porter et al. 2022), we observed radial-like cells extending large processes into layer 2. The persistence of such long glial expansions at later developmental stages has also been described in mice (Lim and Alvarez-Buylla 2016) and dogs (Fernández-Flores et al. 2018), whereas in rabbits and humans, long radial processes are restricted to early developmental stages (Paredes et al. 2016; G. Ponti et al. 2006).

Despite the high density of glial processes, the subependymal layer is not acellular. In the juvenile swine, layer 2 contains densely packed DCX$^+$ neuroblast clusters, whose cells exhibit ultrastructural features indicative of migration, including condensed chromatin, slightly irregular nuclei, reduced cytoplasm, and microtubule-rich cytoplasmic projections. These clusters are surrounded by astrocyte processes but lack complete isolation, occasionally contacting unmyelinated axons. This organization resembles that found in rabbits (G. Ponti et al. 2006), rather than the compact glial tubes observed in mice (Lois et al. 1996).

In newborn humans, the subependymal layer initially contains numerous neuroblasts, but these rapidly decline within the first year of life, leaving a hypocellular or "gap" layer (Paredes et al. 2016). Similar age-dependent neuroblast reductions have been reported in rabbits (G. Ponti et al. 2006) and swine (Costine et al. 2015; Porter et al. 2022). Other young mammals, including cattle (Rodríguez-Pérez et al. 2003), sheep (Lévy et al. 2017), and primates (Sawamoto et al. 2011), exhibit a V-SVZ organization reminiscent of the hypocellular layer described in humans. This might suggest that layer 2 in swine may develop into a similar gap layer in adulthood, albeit with a slower progression.

In mice, type B cells serve as primary neuronal precursors, giving rise to type C cells, which subsequently generate migrating neuroblasts (type A cells) (Doetsch et al. 1997). In swine, we identified type B and type A cells by TEM; however, we did not observe type C cells with ultrastructural characteristics akin to those described in mice. Consistent with its neurogenic function, layer 2 exhibited Ki-67 expression, indicating active cell proliferation. However, it remains unclear whether this proliferation arises from type B or type A cells, or from unrelated proliferative cell types. In humans, DCX$^+$ chains have been described in the layer 2, but they decline rapidly after 18 months of age, developing a GAP layer (N. Sanai et al. 2011), whereas in swine, they persist into juvenile stages (Porter et al. 2022).

The abventricular region (layer 3) was subdivided based on the occurrence and size of DCX$^+$ clusters. Sublayer 3a, adjacent to the ventricular region, contains small, sparsely distributed DCX$^+$ clusters and isolated DCX$^+$ cells. Sublayer 3b comprises larger DCX$^+$ clusters associated with blood vessels in the dorsal region of the V-SVZ. This pattern of multifocal DCX$^+$ aggregates resembles that observed in rabbits (G. Ponti et al. 2006), while in humans, DCX is observed just until 1 postnatal week in the area that will become the astrocytic ribbon (N. Sanai et al. 2011).

While Ki-67 expression was also detected in layer 3, it was not only associated with neuroblast chains. Considering that the abventricular region of *Sus scrofa* is highly myelinated at 3–5 months, and the documented increase in myelinated fibers has

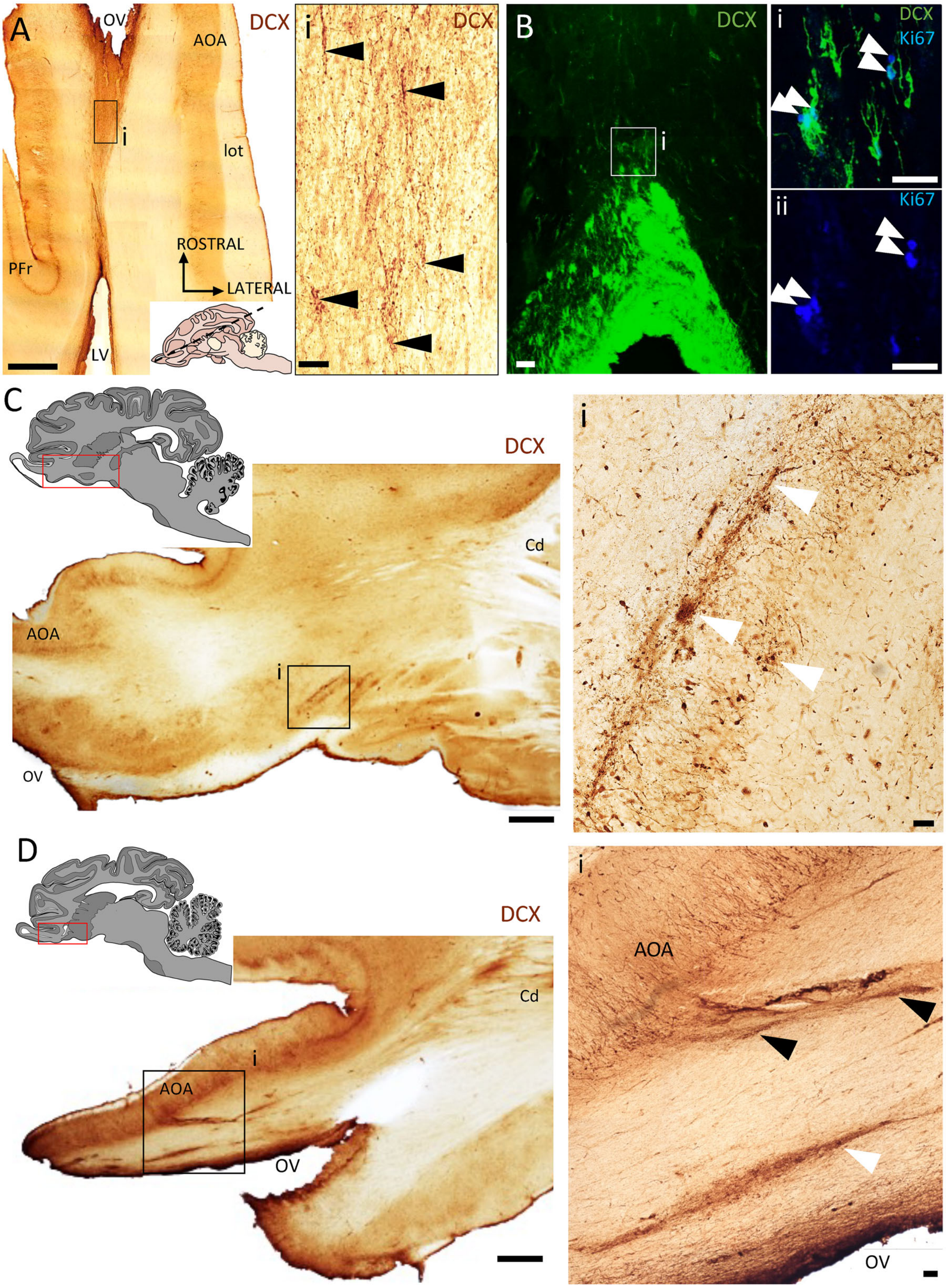

FIGURE 6 | Cell migration toward the olfactory ventricle. (A) DAB immunostaining for DCX in a horizontal section of the swine brain reveals DCX$^+$ chains (i, arrowheads) located between the V-SVZ and the opening of the olfactory bulb ventricle. (B) Immunofluorescence for DCX and Ki-67 shows proliferating cells within some of the chains emerging from the V-SVZ. (C) In sagittal sections, DCX$^+$ chains (arrowheads) are observed near the opening of the olfactory bulb ventricle (i). (D) In addition to their presence near the olfactory ventricle (i, white arrowhead), DCX$^+$ chains are also seen migrating toward the anterior olfactory area (AOA) (i, black arrowheads). Scale bars: 1 mm (A, C, D) and 50 µm (Ai, Bi, Bii, Ci, Di).

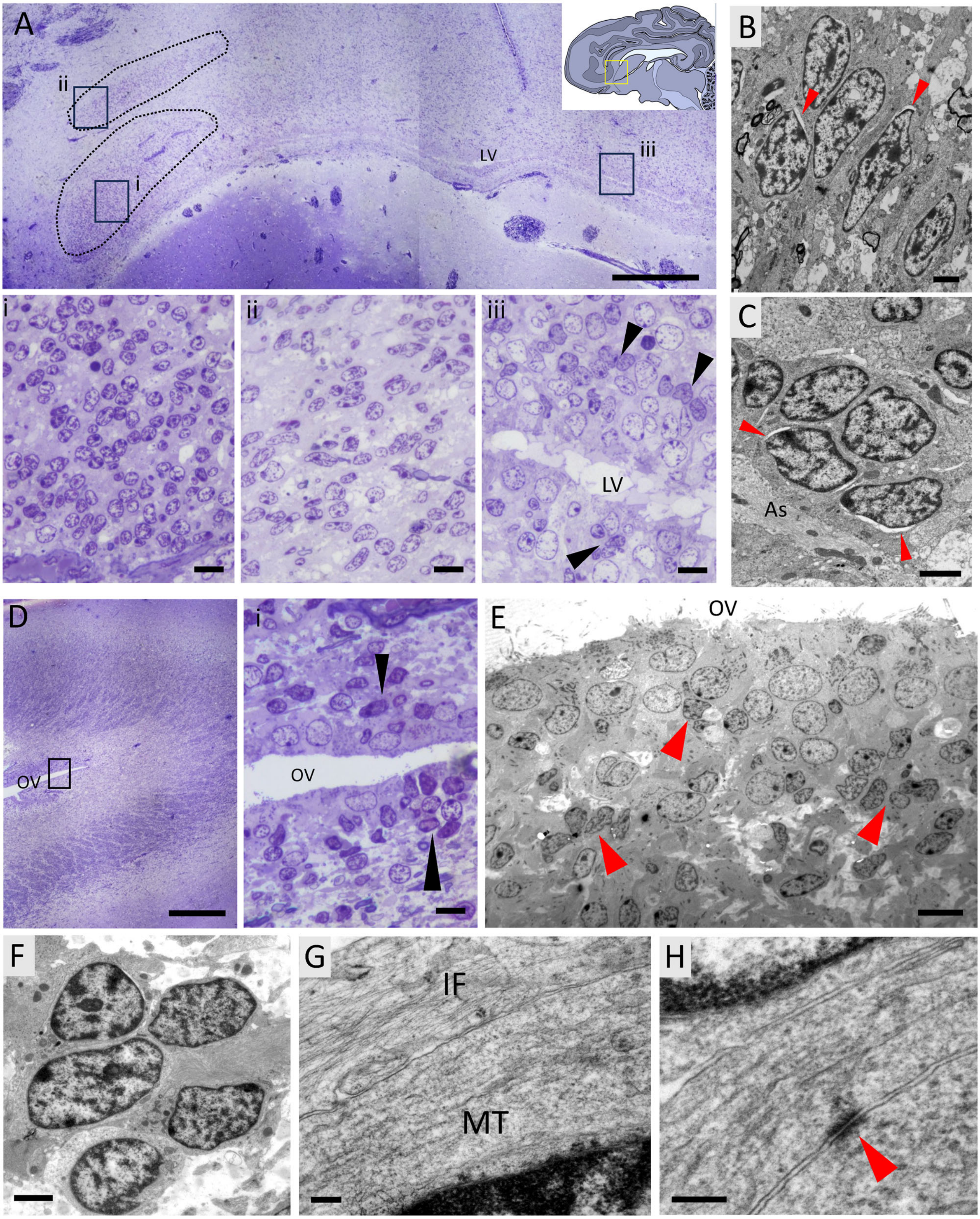

FIGURE 7 | Ultrastructure of neuroblasts along the migratory pathway and at the olfactory ventricle. (A) Semithin section stained with toluidine blue showing two groups of large neuroblast chains (i, ii) migrating rostrally from the V-SVZ, as well as smaller chains near the lateral ventricle wall (iii). Arrowheads indicate neuroblasts adjacent to the ventricle. (B, C) TEM images of clusters of migrating neuroblasts located either within the leading migratory stream (B) or near the ventricle (C). These cells share ultrastructural features such as irregular nuclei, clumped chromatin, reduced cytoplasm, and microtubule-containing processes. Intercellular spaces (arrowheads) are also evident. (D) Semithin section of the olfactory ventricle opening showing chains (i) of migratory-like cells (arrowheads) adjacent to the ventricle wall. (E) TEM image of neuroblast clusters near the olfactory ventricle. (F) Their ultrastructure resembles that of neuroblasts in the V-SVZ, displaying irregular nuclei, clumped chromatin, reduced cytoplasm, and microtubule-rich processes. (G) These processes are filled with microtubules (MT) and are surrounded by astrocytic expansions containing intermediate

filaments (IF). (H) Neuroblasts establish adherens junctions with one other (arrowhead). Scale bars: 500 μm (A, D); 10 μm (Ai, Aii, Aiii, Di, E); 2 μm (B, C, F); and 200 nm (G, H).

been described from 2 to 6 months in miniswine (Fang et al. 2005), it is plausible that the Ki-67 expression in sublayers 3a and 3b may also reflect ongoing neurogenesis and oligodendrogenesis.

DCX$^+$ cells within layer 3 of the swine have been identified as migrating young GABAergic interneurons (Porter et al. 2022). Ultrastructural analysis of the clusters shows features of migratory immature neurons, with irregular nuclei, clumped chromatin, reduced cytoplasm, and intercellular spaces. These characteristics align with those observed in type A cells of other species, including mice (García-Verdugo et al. 2002; Lois et al. 1996), rabbit (G. Ponti et al. 2006), dog (Fernández-Flores et al. 2018), marmoset (Sawamoto et al. 2011), macaques (Gil-Perotin et al. 2009), and young humans (N. Sanai et al. 2011), all of which exhibit similar features indicative of migratory phenotype, and are also similar to DCX$^+$ cells observed in layer 2.

To investigate the potential influence of the V-SVZ's layered structure on migration, we analyzed sagittal sections. Neuroblast clusters in layer 2 exhibited no significant alterations in shape or orientation. However, clusters in sublayer 3a displayed a radial alignment relative to the ventricular lumen. This observation suggests that neuroblasts might originate in layer 2 and migrate tangentially into sublayer 3a as small clusters, subsequently coalescing into the larger clusters observed in sublayer 3b. This pattern suggests that the ventricular region is the primary source of new neuroblasts, while the abventricular zone provides a transient environment for cell aggregation before their migration to other brain regions.

The RMS extends in a caudorostral direction and serves as the primary pathway for neuroblasts migrating from the V-SVZ to the olfactory bulb. Migration through the RMS has been extensively documented in various species, including macaque (Gil-Perotin et al. 2009), marmoset (Sawamoto et al. 2011), piglet (Costine et al. 2015), and human (Paredes et al. 2016; N. Sanai et al. 2011). In juvenile swine, neuroblasts from layer 2 of the V-SVZ primarily migrate via the RMS to supply new cells to the olfactory bulb, as evidenced by the presence of DCX$^+$ clusters in the subependymal layer along all the ventricular extension. Consistent with species possessing a highly developed sense of smell, such as rabbits and dogs, the OVs in swine do not close at birth and are continuous with the LV (Fasolo et al. 2002).

Neuroblasts within the RMS exhibited ultrastructural features of immature migrating neurons, including irregular nuclei, clumped chromatin, limited cytoplasm, and noticeable intercellular spaces. However, in the vicinity of the OV, neuroblasts no longer form large chains but rather small, densely packed clusters interspersed with astrocytes. Intercellular spaces were not observed, and cells exhibited adherens junctions between them. While glial tubes facilitate neuroblast migration in rodents (Lois et al. 1996), the prominent neuroblast chains and clusters observed in the juvenile swine brain may represent an adaptation that supports long-distance migration in the context of less well-organized glial scaffolds.

Ki-67 staining revealed proliferation within DCX$^+$ clusters migrating toward the OB. In mice, neuroblasts migrating from the V-SVZ along the RMS retain the capacity to divide (G. P. Ponti et al. 2013), and similar proliferation has been observed throughout the RMS up to the olfactory peduncle in dogs (Malik et al. 2012).

Furthermore, large clusters from layer 3b are more prevalent in anterior coronal sections than in posterior regions. This might suggest a caudal-to-rostral migration pattern (Porter et al. 2022) of layer 3 neuroblasts parallel to the RMS. Following the trajectory of this alternative stream, we observed chains of DCX$^+$ cells migrating toward cortical areas reaching, for instance, the anterior olfactory area. We also observed clusters deviating ventrally, probably toward the olfactory bulb. Some of these alternative branches have been previously described in young piglets at 14 postnatal days (Costine et al. 2015). Studies in other mammalian species have also reported small clusters or individual cells migrating through additional routes in the telencephalon, indicating the potential existence of alternative migratory pathways beyond the RMS (Bonfanti and Ponti 2008; De Marchis et al. 2004; Paredes et al. 2016).

5 | Conclusion

Our findings provide a comprehensive characterization of the cellular architecture and migration pathways within the juvenile swine V-SVZ, reinforcing the structural and functional similarities between this neurogenic niche and those described in other mammalian species. The juvenile swine emerges as a relevant model for investigating neurogenesis in large-brained mammals, offering insights into the organization, cellular dynamics, and potential regulatory mechanisms of the V-SVZ that may inform studies of human brain development. While the structural similarities between the swine and human V-SVZ suggest potential parallels, our study highlights both shared and species-specific features, refining the current understanding of this neurogenic niche. Rather than assuming direct extrapolation to human neurogenesis, our work establishes a foundation for comparative analyses by redefining the layered architecture of the juvenile swine V-SVZ and detailing the spatial distribution of its cellular components. Future studies integrating molecular profiling and lineage-tracing approaches will be essential to elucidate the conserved and divergent aspects of neurogenesis across species and to explore how the swine model may contribute to the development of regenerative strategies for neurological disorders.

Author Contributions

L.I.T.-S. contributed to the experimental design, conducted experiments, analyzed data, and wrote the first draft of the manuscript. J.F. performed immunohistochemical analyses and assisted in data interpretation. E.D. and L.M. provided the study samples and contributed to their characterization. K.S. participated in the interpretation of results and contributed

to critical revisions. L.T.-S., J.M.G.-V., and V.H.-P. conceived and designed the study. J.M.G.-V. and V.H.-P. supervised the project, secured funding, provided critical revisions, and approved the final manuscript. All authors reviewed and approved the final manuscript.

Acknowledgments

L.I.T.-S. has a predoctoral contract by the Valencian Council for Education, Universities and Employment (ACIF2021/420). J.F. has a predoctoral FPU contract by the Spanish Council for Education, Professional Education and Sports (FPU22/03133). This work was supported by the Valencian Council for Education, Culture, University and Employment (CIPROM/2023/053) to J.M.G.-V. and V.H.-P., as well as the Core-to-Core Program of the Japan Society for the Promotion of Science (JPJSCCA20230007) to J.M.G.-V., V.H.-P., and K.S. and a Grant-in-Aid for Outstanding Research Group Support in Nagoya City University (2401101) to K.S. Furthermore, this project is also funded by the Spanish Ministerio de Ciencia, Innovación y Universidades and Agencia Estatal de Investigación, MICIU/AEI/10.13039/501100011033 and FEDER-EU (grant no. PID2023-151927OB-I00 to L.M. and E.D.), and by the AGAUR/Generalitat de Catalunya (2021 SGR 01359 to L.M.).

Ethics Statement

We declare that we adhere to the ethical and integrity policies of the journal regarding research. All the protocols used were approved by the Committees of Ethics for Animal Experimentation and Biosecurity of the University of Lleida and by the Generalitat de Catalunya.

Conflicts of Interest

The authors declare no conflicts of interest.

Data Availability Statement

The data that support the findings of this study are available from the corresponding author upon reasonable request.

References

Altman, J. 1969. "Autoradiographic and Histological Studies of Postnatal Neurogenesis. IV. Cell Proliferation and Migration in the Anterior Forebrain, With Special Reference to Persisting Neurogenesis in the Olfactory Bulb." *The Journal of Comparative Neurology* 137, no. 4: 433–457. https://doi.org/10.1002/CNE.901370404.

Alvarez-Buylla, A., and J. M. García-Verdugo. 2002. "Neurogenesis in Adult Subventricular Zone." *The Journal of Neuroscience* 22, no. 3: 629–634. https://doi.org/10.1523/JNEUROSCI.22-03-00629.2002.

Bonfanti, L., and G. Ponti. 2008. "Adult Mammalian Neurogenesis and the New Zealand White Rabbit." *Veterinary Journal* 175, no. 3: 310–331. https://doi.org/10.1016/j.tvjl.2007.01.023.

Casalia, M. L., T. Li , H. Ramsay , P. J. Ross , M. F. Paredes , and S. C. Baraban. 2021. "Interneuron Origins in the Embryonic Porcine Medial Ganglionic Eminence." *The Journal of Neuroscience* 41, no. 14: 3105–3119. https://doi.org/10.1523/JNEUROSCI.2738-20.2021.

Cebrian-Silla, A., M. Assis Nascimento , W. Mancia , et al. 2024. "Neural Stem Cell Relay from B1 to B2 Cells in the Adult Mouse Ventricular-Subventricular Zone." Preprint, bioRxiv, July 9. https://doi.org/10.1101/2024.06.28.600695.

Costine, B. A., S. Missios , S. R. Taylor , et al. 2015. "The Subventricular Zone in the Immature Piglet Brain: Anatomy and Exodus of Neuroblasts Into White Matter After Traumatic Brain Injury." *Developmental Neuroscience* 37, no. 2: 115–130. https://doi.org/10.1159/000369091.

De Marchis, S., A. Fasolo , and A. C. Puche. 2004. "Subventricular Zone-Derived Neuronal Progenitors Migrate Into the Subcortical Forebrain of Postnatal Mice." *Journal of Comparative Neurology* 476, no. 3: 290–300. https://doi.org/10.1002/CNE.20217.

Doetsch, F., I. Caille , D. A. Lim , J. M. Garcia-Verdugo , and A. Alvarez-Buylla. 1999. "Subventricular Zone Astrocytes Are Neural Stem Cells in the Adult Mammalian Brain." *Cell* 97, no. 6: 703–716. https://doi.org/10.1016/S0092-8674(00)80783-7.

Doetsch, F., J. M. García-Verdugo , and A. Alvarez-Buylla. 1997. "Cellular Composition and Three-Dimensional Organization of the Subventricular Germinal Zone in the Adult Mammalian Brain." *The Journal of Neuroscience* 17, no. 13: 5046–5061. https://doi.org/10.1523/JNEUROSCI.17-13-05046.1997.

Fang, M., J. Li , X. Gong , et al. 2005. "Myelination of the Pig's Brain: A Correlated MRI and Histological Study." *Neuro-Signals* 14, no. 3: 102–108. https://doi.org/10.1159/000086292.

Fasolo, A., P. Peretto , and L. Bonfanti. 2002. "Cell Migration in the Rostral Migratory Stream." *Chemical Senses* 27, no. 6: 581–582. https://doi.org/10.1093/CHEMSE/27.6.581.

Fernández-Flores, F., J. M. García-Verdugo , R. Martín-Ibáñez , et al. 2018. "Characterization of the Canine Rostral Ventricular-Subventricular Zone: Morphological, Immunohistochemical, Ultrastructural, and Neurosphere Assay Studies." *The Journal of Comparative Neurology* 526, no. 4: 721–741. https://doi.org/10.1002/CNE.24365.

García-Verdugo, J. M., S. Ferrón , N. Flames , L. Collado , E. Desfilis , and E. Font. 2002. "The Proliferative Ventricular Zone in Adult Vertebrates: A Comparative Study Using Reptiles, Birds, and Mammals." *Brain Research Bulletin* 57, no. 6: 765–775. https://doi.org/10.1016/S0361-9230(01)00769-9.

Giedd, J. N., M. Keshavan , and T. Paus. 2008. "Why do many psychiatric disorders emerge during adolescence?" *Nature Reviews in Neuroscience* 9, no. 12: 947–957. https://doi.org/10.1038/nrn2513.

Gil-Perotin, S., M. Duran-Moreno , S. Belzunegui , M. R. Luquin , and J. M. Garcia-Verdugo. 2009. "Ultrastructure of the Subventricular Zone in Macaca Fascicularis and Evidence of a Mouse-Like Migratory Stream." *The Journal of Comparative Neurology* 514, no. 5: 533–554. https://doi.org/10.1002/CNE.22026.

Kempermann, G., H. Song , and F. H. Gage. 2015. "Neurogenesis in the Adult Hippocampus." *Cold Spring Harbor Perspectives in Biology* 7, no. 9: a018812. https://doi.org/10.1101/CSHPERSPECT.A018812.

Lévy, F., M. Batailler , M. Meurisse , and M. Migaud. 2017. "Adult Neurogenesis in Sheep: Characterization and Contribution to Reproduction and Behavior." *Frontiers in Neuroscience* 11: 570. https://doi.org/10.3389/FNINS.2017.00570.

Lim, D. A., and A. Alvarez-Buylla. 2016. "The Adult Ventricular–Subventricular Zone (V-SVZ) and Olfactory Bulb (OB) Neurogenesis." *Cold Spring Harbor Perspectives in Biology* 8, no. 5: a018820. https://doi.org/10.1101/CSHPERSPECT.A018820.

Lois, C., and A. Alvarez-Buylla. 1994. "Long-Distance Neuronal Migration in the Adult Mammalian Brain." *Science* 264, no. 5162: 1145–1148. https://doi.org/10.1126/SCIENCE.8178174.

Lois, C., J. M. García-Verdugo , and A. Alvarez-Buylla. 1996. "Chain Migration of Neuronal Precursors." *Science* 271, no. 5251: 978–981. https://doi.org/10.1126/SCIENCE.271.5251.978.

Low, V. F., R. L. M. Faull , L. Bennet , A. J. Gunn , and M. A. Curtis. 2013. "Neurogenesis and Progenitor Cell Distribution in the Subgranular Zone and Subventricular Zone of the Adult Sheep Brain." *Neuroscience* 244: 173–187. https://doi.org/10.1016/j.neuroscience.2013.04.006.

Malik, S. Z., M. Lewis , A. Isaacs , et al. 2012. "Identification of the Rostral Migratory Stream in the Canine and Feline Brain." *PLoS ONE* 7, no. 5: e36016. https://doi.org/10.1371/JOURNAL.PONE.0036016.

Mirzadeh, Z., Y. Kusne , M. Duran-Moreno , et al. 2017. "Bi- and Uniciliated Ependymal Cells Define Continuous Floor-Plate-Derived Tanycytic Territories." *Nature Communications* 8: 13759. https://doi.org/10.1038/ncomms13759.

Nogueira, A. B., M. C. Sogayar , A. Colquhoun , et al. 2014. "Existence of a Potential Neurogenic System in the Adult Human Brain." *Journal of Translational Medicine* 12: 75. https://doi.org/10.1186/1479-5876-12-75.

Paredes, M. F., D. James , S. Gil-Perotin , et al. 2016. "Extensive Migration of Young Neurons Into the Infant Human Frontal Lobe HHS Public Access." *Science* 354, no. 6308. https://doi.org/10.1126/science.aaf7073.

Ponti, G., P. Aimar , and L. Bonfanti. 2006. "Cellular Composition and Cytoarchitecture of the Rabbit Subventricular Zone and Its Extensions in the Forebrain." *Journal of Comparative Neurology* 498, no. 4: 491–507. https://doi.org/10.1002/CNE.21043.

Ponti, G. P., K. Obernier , and A. Alvarez-Buylla. 2013. "Lineage Progression From Stem Cells to New Neurons in the Adult Brain Ventricular-Subventricular Zone." *Cell Cycle* 12, no. 11: 1649–1650. https://doi.org/10.4161/CC.24984.

Porter, D. D. L., S. N. Henry , S. Ahmed , et al. 2022. "Neuroblast Migration Along Cellular Substrates in the Developing Porcine Brain." *Stem Cell Reports* 17, no. 9: 2097–2110. https://doi.org/10.1016/J.STEMCR.2022.07.015.

Quiñones-Hinojosa, A., N. Sanai , M. Soriano-Navarro , et al. 2006. "Cellular Composition and Cytoarchitecture of the Adult Human Subventricular Zone: A Niche of Neural Stem Cells." *Journal of Comparative Neurology* 494, no. 3: 415–434. https://doi.org/10.1002/CNE.20798.

Rodríguez-Pérez, L. M., M. Pérez-Martín , A. J. Jiménez , and P. Fernández-Llebrez. 2003. "Immunocytochemical Characterisation of the Wall of the Bovine Lateral Ventricle." *Cell and Tissue Research* 314, no. 3: 325–335. https://doi.org/10.1007/S00441-003-0794-1.

Sanai, H., A. D. Tramontin , A. Quiñones-Hinojosa , et al. 2004. "Unique Astrocyte Ribbon in Adult Human Brain Contains Neural Stem Cells but Lacks Chain Migration." *Nature* 427, no. 6976: 740–744. https://doi.org/10.1038/nature02301.

Sanai, N., T. Nguyen , R. A. Ihrie , et al. 2011. "Corridors of Migrating Neurons in Human Brain and Their Decline During Infancy." *Nature* 478, no. 7369: 382–386. https://doi.org/10.1038/NATURE10487.

Sawamoto, K., Y. Hirota , C. Alfaro-Cervello , et al. 2011. "Cellular Composition and Organization of the Subventricular Zone and Rostral Migratory Stream in the Adult and Neonatal Common Marmoset Brain." *The Journal of Comparative Neurology* 519, no. 4: 690–713. https://doi.org/10.1002/CNE.22543.

Tong, C. K., J. Chen , A. Cebrián-Silla , et al. 2014. "Axonal Control of the Adult Neural Stem Cell Niche." *Cell Stem Cell* 14, no. 4: 500–511. https://doi.org/10.1016/J.STEM.2014.01.014.